

Tolerance to geometrical inaccuracies in CBCT systems: A comprehensive study

Monica Abella^{1,2,3} | Cristobal Martinez^{1,2} | Ines Garcia² | Patricia Moreno^{1,2} |
Claudia De Molina² | Manuel Desco^{1,2,3,4}

¹Dept. Bioingeniería e Ingeniería Aeroespacial, Universidad Carlos III de Madrid, Madrid, Spain

²Instituto de Investigación Sanitaria Gregorio Marañón, Madrid, Spain

³Centro Nacional de Investigaciones Cardiovasculares Carlos III (CNIC), Madrid, Spain

⁴Centro de Investigación Biomédica en Red de Salud Mental (CIBERSAM), Madrid, Spain

Correspondence

Monica Abella, Departamento de Bioingeniería e Ingeniería Aeroespacial, Universidad Carlos III de Madrid, Avda. de la Universidad 30, 28911 Leganés, Madrid, Spain.
Email: mabella@ing.uc3m.es

Funding information

Centro Nacional de Investigaciones Cardiovasculares (CNIC); Comunidad de Madrid (Community of Madrid); Ministerio de Economía y Competitividad, Grant/Award Number: DPI2016-79075-R; Instituto de Salud Carlos III; European Regional Development Fund; CRUE Universidades; CSIC; Banco Santander; Ministerio de Ciencia, Innovación y Universidades

Abstract

Purpose: The last decades have seen the consolidation of the cone-beam CT (CBCT) technology, which is nowadays widely used for different applications such as micro-CT for small animals, mammography, dentistry, or surgical procedures. Some CBCT systems may suffer mechanical strains due to the heavy load of the x-ray tube. This fact, together with tolerances in the manufacturing process, lead to different types of undesirable effects in the reconstructed image unless they are properly accounted for during the reconstruction. To obtain good quality images, it is necessary to have a complete characterization of the system geometry including the angular position of the gantry, the source–object and detector–object distances, and the position and pose of the detector. These parameters can be obtained through a calibration process done periodically, depending on the stability of the system geometry. To the best of our knowledge, there are no comprehensive works studying the effect of inaccuracies in the geometrical calibration of CBCT systems in a systematic and quantitative way. In this work, we describe the effects of detector misalignments (linear shifts, rotation, and inclinations) on the image and define their tolerance as the maximum error that keeps the image free from artifacts.

Methods: We used simulations of four phantoms including systematic and random misalignments. Reconstructions of these data with and without errors were compared to identify the artifacts introduced in the reconstructed image and the tolerance to miscalibration deemed to provide acceptable image quality.

Results: Visual assessment provided an easy guideline to identify the sources of error by visual inspection of the artifactual images. Systematic errors result in blurring, shape distortion and/or reduction of the axial field of view while random errors produce streaks and blurring in all cases, with a tolerance which is more than twice that of systematic errors. The tolerance corresponding to errors in position of the detector along the tangential direction, that is, skew ($<0.2^\circ$) and horizontal shift (<0.4 mm), is tighter than the tolerance to those errors affecting

Monica Abella and Cristobal Martinez contributed equally to this work.

This is an open access article under the terms of the Creative Commons Attribution-NonCommercial-NoDerivs License, which permits use and distribution in any medium, provided the original work is properly cited, the use is non-commercial and no modifications or adaptations are made.

© 2021 The Authors. *Medical Physics* published by Wiley Periodicals LLC on behalf of American Association of Physicists in Medicine

the position along the longitudinal direction or the magnification, that is, vertical shift (<2 mm), roll (<1.5°), tilt (<2°), and SDD (<3 mm).

Conclusion: We present a comprehensive study, based on realistic simulations, of the effects on the reconstructed image quality of errors in the geometrical characterization of a CBCT system and define their tolerance. These results could be used to guide the design of new systems, establishing the mechanical precision that must be achieved, and to help in the definition of an optimal geometrical calibration process. Also, the thorough visual assessment may be valuable to identify the most predominant sources of error based on the effects shown in the reconstructed image.

KEYWORDS

artifact radiography, CBCT, dual energy, misalignment

1 | INTRODUCTION

Cone-beam CT (CBCT) is a technology that experienced a substantial increase with the advent of flat-panel detectors. The potential clinical use of the CBCT was demonstrated for the first time in the Mayo Clinic in 1982.¹ Initially intended for angiography,^{1–3} it is nowadays not only used for many clinical and preclinical applications such as micro-tomography for small animal,^{4,5} radiotherapy guidance,^{6,7} mammography,^{8,9} dentistry imaging,^{10,11} and general surgical procedures, mainly for head and neck but also in spinal, thoracic, abdominal, and orthopedic interventions.^{12–16} CBCT hardware settings include U-arms, O-arms, and C-arms, either fixed or mobile.¹⁴

C-arms usually describe non-isocentric trajectories due to the slipping of the arm on the base. This fact, together with the tolerances derived from the manufacturing process, lead to deviations from the expected circular orbit. They may also be subjected to mechanical strains, like arm flexion due to the heavy loads at its end, resulting in changes of the relative positions between source and detector for different projections, which may not be repeatable through consecutive experiments. We may also find errors in the angular position of the source–detector pair due to inaccuracies of the positioning system used.

If these non-idealities are not properly considered during reconstruction, the resulting images become contaminated with undesirable effects such as blurring, changes in size, or geometrical distortion. For this reason, it is essential to fully characterize the geometry of the system through a calibration process.

To the best of our knowledge, there are only a few works evaluating the effect of errors in the geometrical calibration of a CBCT system and the tolerances for each geometrical parameter (in terms of mechanical precision) in a systematic and quantitative way. In Daly et al.,¹⁷ the authors evaluated the effects of random

and systematic errors on the reconstructed image. However, the study was not comprehensive, limited to four error values for each geometrical parameter of a specific C-arm system and without giving an accurate tolerance value (threshold for which the errors become noticeable in the reconstructed image). Ferrucci et al.¹⁸ evaluated only the detector angular misalignments. Muralikrishnan et al.¹⁹ proposed a method to evaluate the effects of misalignments, involving a phantom composed of spheres, but did not study the effect of random misalignments or propose a tolerance value. Finally, no work in the literature presents a thorough visual assessment of the effects in the reconstructed image.

In this work, we make use of a realistic simulator to present a comprehensive study of the effects of errors in the geometrical parameters for CBCT systems. For each geometrical parameter, we describe the effects produced in the image and estimate its tolerance. We also study the dependence of these effects on the acquisition parameters that affect the spatial resolution, namely, pixel size, angular step, and magnification.

2 | MATERIALS AND METHODS

We simulated the geometry of the C-arm PowerMobil from Siemens Medical Solutions, which makes use of a flat panel detector (active matrix of 2048 × 1536 pixels, with a pixel size of 194 μm and a projection area of 40 × 30 cm²).¹⁷ Figure 1 shows the overall geometry of the system with a magnification factor of 1.97 resulting in a field of view (FOV) of 201 × 201 × 151 mm³ (acquisition protocol 1 in Table 1).

Simulations were carried out using FUX-Sim, a software tool that emulates cone-beam x-ray systems and allows the user to define all possible geometrical non-idealities.²⁰ Geometrical parameters can be described as the detector misalignments shown in

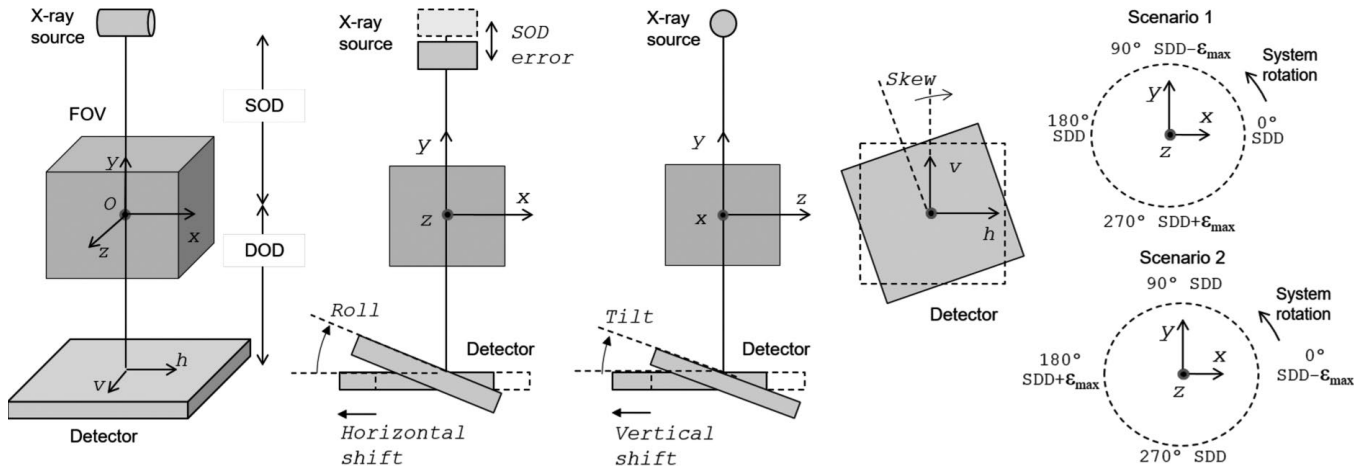


FIGURE 1 Cone-beam geometry used for simulations and definition of the geometrical parameters of the system

TABLE 1 Acquisition protocols tested

Protocol	1	2	3	4	5	6	7	8	9
Span angle	360	360	360	360	360	360	360	360	360
Ang. step (deg)	1	0.5	2	1	0.5	0.25	1	1	1
Pixel size (μm)	776	776	776	388	388	388	1552	776	776
Voxel size (μm)	394	394	394	197	197	197	788	485	646
Magnification	1.97	1.97	1.97	1.97	1.97	1.97	1.97	1.6	1.2

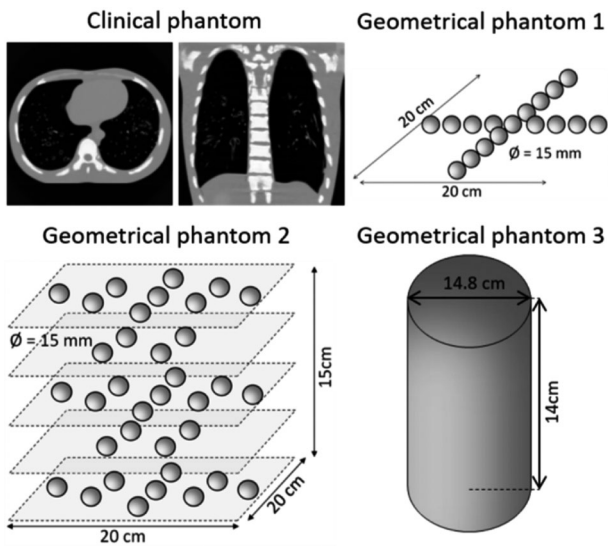


FIGURE 2 Phantoms used for image quality evaluation

Figure 1: displacements of the detector in the vertical and horizontal directions (shift), rotation of the flat panel with respect to its central point (skew), and inclinations with respect to its vertical and horizontal axes (roll and tilt, respectively). Any misalignment of the x-ray source can also be translated to a detector misalignment. Variations in the source–detector distance (SDD) can be described as changes in the

source–object distance (SOD) or variations in the detector–object distance (DOD), both of which would result in similar effects on the reconstructed image. Here, we use the former option to account for SDD errors since the source is usually the heaviest element on the arm.

Projections were simulated under realistic conditions, including two types of errors in each geometrical parameter: (1) systematic errors, equal for all projection angles, and (2) random errors, uniformly distributed with mean zero, to account for angle-dependent variations in detector geometry. Random errors were tested five times. We also studied the errors in SDD proportional to gantry angle, since this can be an effect produced by the weight of the x-ray tube. To this end, we simulated the two scenarios depicted in the rightmost panel of Figure 1, for two different initial angles, with an error that increases linearly from 0 up to ϵ_{max} .

Simulations were carried out using the four phantoms depicted in Figure 2:

- Clinical phantom: Data from a CT study of the anthropomorphic chest phantom PBU-60, manufactured by Kyoto Kagaku (voxel size 0.394 mm isotropic) for visual evaluation
- Geometrical phantom 1: A synthetic phantom comprising 18 spheres of 15 mm diameter (voxel size 0.134 mm isotropic), to enhance certain effects in the visual evaluation.

- Geometrical phantom 2: A synthetic phantom comprising 35 spheres of 15 mm diameter distributed in five slices (voxel size 0.134 mm isotropic), designed for quantitative evaluation of undesirable effects at different points of the FOV, similar to the one proposed by Muralikrishnan.¹⁹
- Geometrical phantom 3: A synthetic phantom resembling a homogeneous cylinder of 148 mm diameter (voxel size 0.134 mm isotropic), intended for the quantitative evaluation of the dependency of the undesirable effects with the distance to the center of the FOV.

Two reconstructions were obtained from these data: (1) a calibrated reconstruction, considering the true value of the geometrical parameters (as it would happen with a properly calibrated system) and (2) an inaccurate reconstruction, ignoring the geometrical non-idealities. We compared calibrated and inaccurate reconstructions following two steps. In the first step, we used the clinical phantom (chest) and the geometrical phantom 1 (spheres) to identify the effects on the image and find a first approximation to its tolerance by visual assessment. To this end, we tested a wide range of error values for each parameter, based on the values used by Daly et al.¹⁷ In a second step, we refined the first estimation of the tolerance obtained visually, by testing error values with a smaller step. The resulting artifacts, namely blurring, change in size, and image distortion, were quantified in the three views (axial, coronal, and sagittal). We used geometrical phantom 2 (spheres) to evaluate blurring and geometrical phantom 3 (cylinder) to evaluate image distortion and size changes.

The effect on the reconstructed image was quantitatively assessed as:

$$\text{Effect} = |\text{FW20}_{\text{inaccurate}} - \text{FW20}_{\text{ideal}}|,$$

where $\text{FW20}_{\text{inaccurate}}$ and $\text{FW20}_{\text{ideal}}$ are the diameter in the inaccurate reconstruction and the calibrated reconstruction, respectively, which are calculated as the width at 20% of full peak value, over profiles taken in the vertical, horizontal, and two diagonal directions.

We considered an undesirable effect to be present when it is noticeable in the reconstructed image, that is, when it is higher than one voxel. The tolerance, ϵ_{tol} , was then quantified as the maximum error, in millimeters or degrees that does not exceed this threshold. For errors that depend on the distance to the FOV center, we show the results at 47.28 mm from this point (~50% of the FOV) and used the cylinder phantom to evaluate this dependency with the distance to the FOV center. As the effect may also depend on the direction, we quantified the effect for three orientations of the cylinder (axial, coronal, and sagittal).

Due to the wide range of systems based on cone-beam geometry and the trend toward low-dose

acquisition protocols, we evaluated the dependency of the tolerance value with the acquisition parameters that have an influence in the spatial resolution: projection pixel size, angular step (between projections), and magnification. To this end, we repeated the above-described experiments for acquisition protocols 2 to 7 in Table 1.

To evaluate the dependency of the tolerance with pixel size, we used protocols 2, 6, and 7, selecting for each case an optimum value of angular step calculated so that sampling in the angular direction at the edge of the FOV matched radial sampling:

$$\text{pixel_size} = \text{arc_step} \rightarrow \frac{2r}{N_p} = \frac{\pi r}{N_\alpha}$$

where r is the radius of the gantry rotation trajectory, N_p the number of detector pixels, and N_α the number of angular positions.

We studied the dependency of the tolerance with the magnification of the system using protocols 1, 8, and 9, with a magnification value of 1.97, 1.6, and 1.2, respectively.

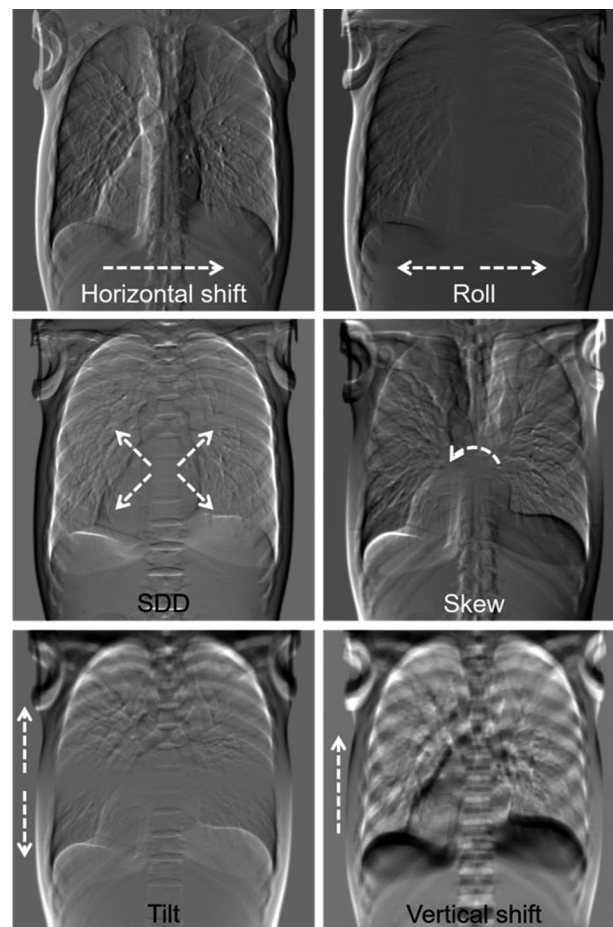


FIGURE 3 Difference image of ideal and misaligned projections of the anthropomorphic phantom for the evaluated geometrical parameters. Protocol 1 (voxel size of 394 μm)

3 | RESULTS

3.1 | Effects of inaccuracies in geometrical parameters for protocol 1

3.1.1 | Visual assessment

Figure 3 shows the difference image between the ideal and misaligned projections for each geometrical parameter evaluated. Linear shifts and rotation of the detector are translated into equivalent shifts and rotation in the projection image. Roll and tilt produce an enlargement of one half of the image and a shrinking

of the other half along the horizontal and vertical directions, respectively. Finally, errors in SDD translate into size changes.

Figures 4 and 5 show the effects of systematic errors on the reconstructed image. Systematic errors in horizontal shift produce a 2D isotropic blurring in the axial slice that is constant across the slices. Systematic errors in roll produce a blurring that increases with the distance to the rotation axis in the axial view, also constant across the slices (see dashed arrows in Figures 4 and 5, and the effect in the balls at different positions in Figure 6, top). Systematic errors in skew produce a 2D isotropic blurring in the axial view that increases with

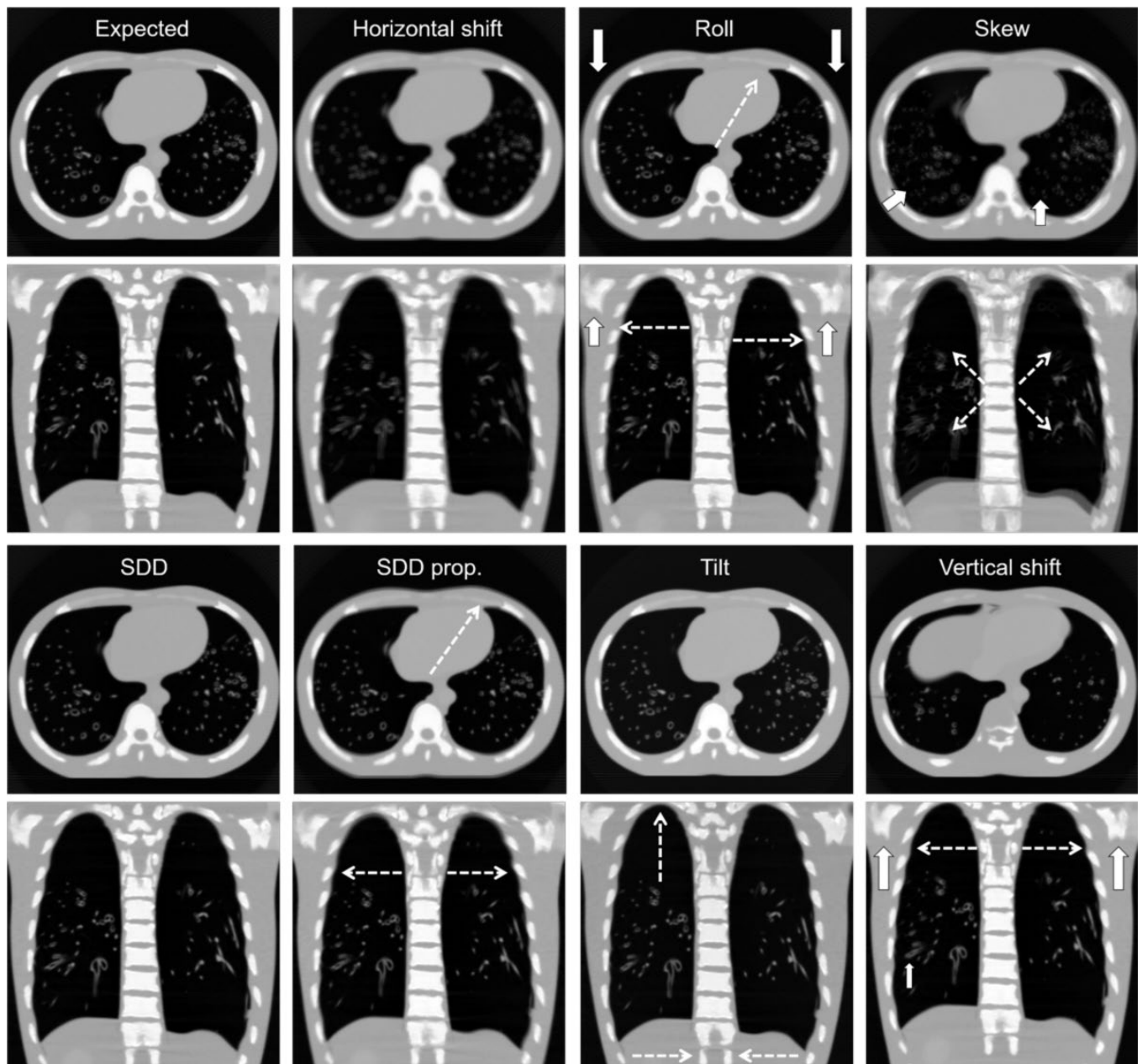


FIGURE 4 Coronal and axial views of the anthropomorphic phantom reconstructed with systematic errors of 15 mm in horizontal shift, 5° in roll, 1.5° in skew, 15 mm in SDD, 10 mm in SDD proportional, 15° in tilt, and 15 mm in vertical shift. Protocol 1 (voxel size of 394 μm)

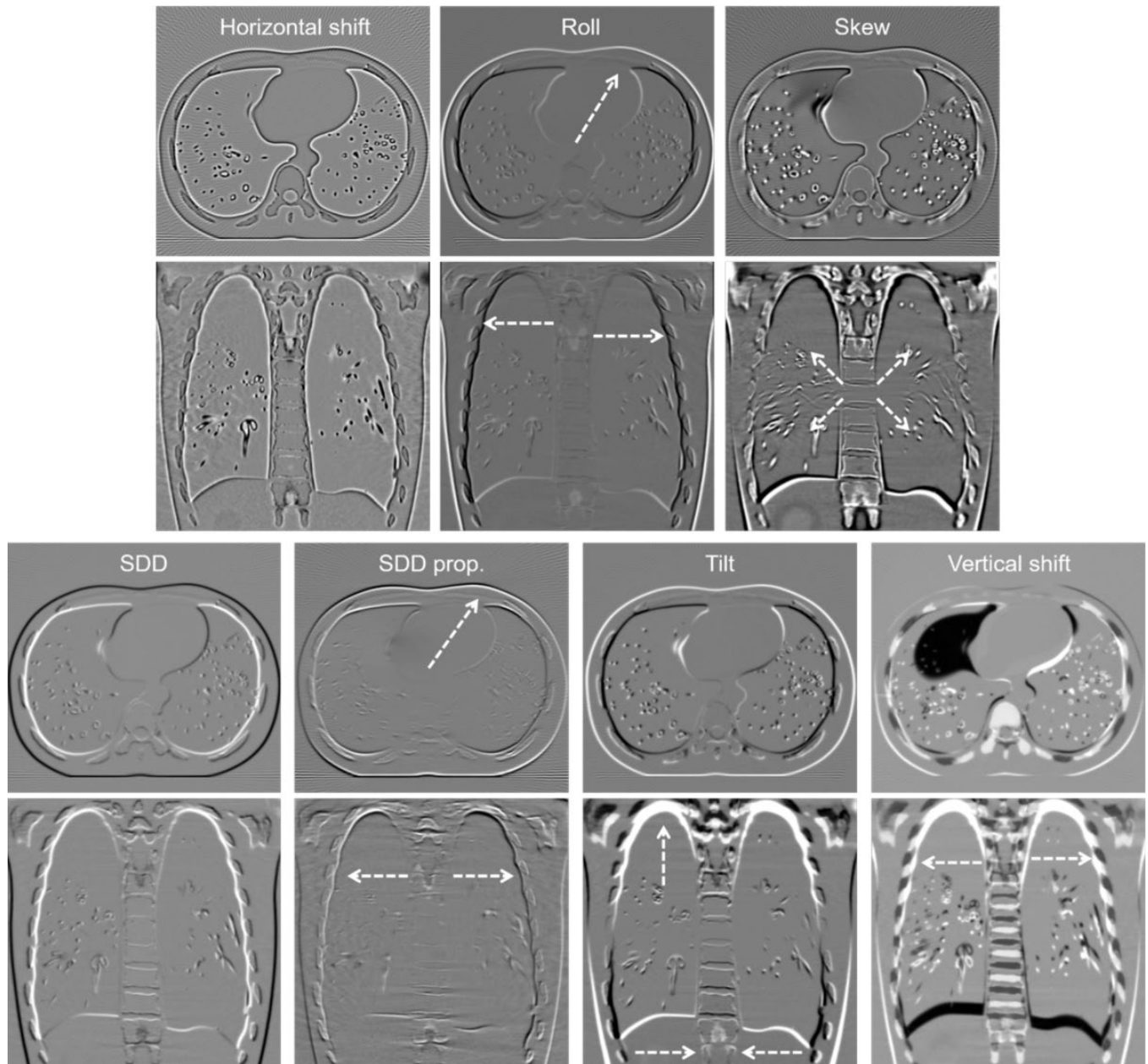


FIGURE 5 Difference of ideal and misaligned reconstructions for errors in Figure 4. Protocol 1 (voxel size of 394 μm)

the distance to the center of the FOV (see dashed arrows in Figures 4 and 5) together with a non-isotropic blurring in longitudinal direction with a mixing of slices (see thick arrows pointing to structures from contiguous slices in Figure 4). Systematic errors in SDD produce a change in voxel size that enlarges or shrinks the object, depending on sign of the error, while errors in tilt produce a distortion, shrinking one half of the object while enlarging the other half in the vertical direction (see dashed arrows in Figures 4 and 5). Systematic errors in SDD proportional to the angular position of the gantry produce a blurring that increases with the distance to the rotation axis, which is higher in the direction perpendicular to the projection angles with higher SDD error

(see Figure 6, center). Errors in vertical shift produce a displacement of the object in the vertical direction as well as vertical blurring constant across the axial slices but increasing its effect with the distance to the rotation axis (see Figure 6, bottom). Table 2 summarizes the main results of the visual assessment.

Figure 7 shows the effect of the random errors in the anthropomorphic phantom; we only show the view where the artifacts are more noticeable. All random errors produce blurring and streaks. This blurring is isotropic in the axial view for horizontal shift and skew, while it increases with the distance to the rotation axis for an error in roll (see dashed arrow in Figure 7). Random

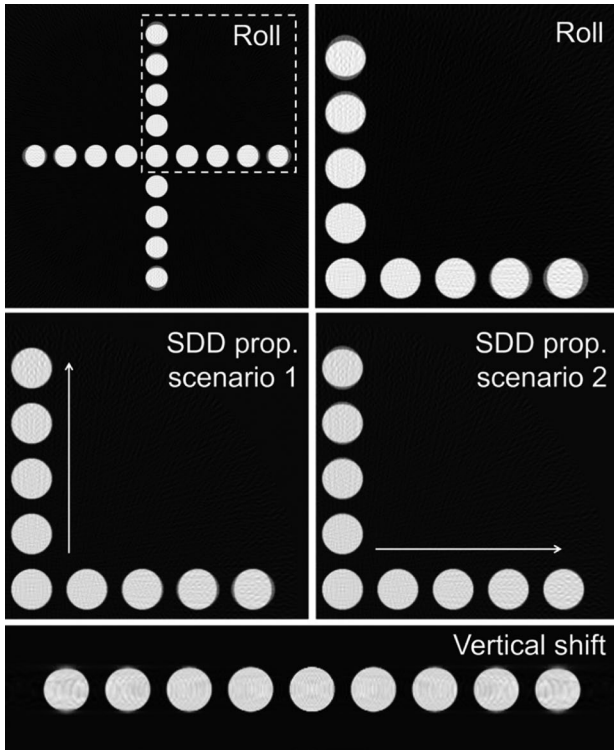


FIGURE 6 Top: Central axial slice of geometrical phantom 1 reconstructed with an error in roll of 5° (left) and zoom corresponding to the dashed square (right). Center: Same zoom for an error of 10 mm in SDD proportional. Bottom: Coronal slice of geometrical phantom 1 reconstructed with an error in vertical shift of 15 mm. Protocol 1 (voxel size of 394 μm)

TABLE 2 Summary of the most predominant sources of error based on visual assessment

Observed effect	View	Likely cause
Shape distortion at top and bottom	Coronal/Sagittal	Tilt
Blurring at right and left	Coronal/Sagittal	Roll
Vertical blurring	Coronal/Sagittal	Vertical shift
Increased blurring from the center	Coronal/Sagittal	Skew
Isotropic blurring	Axial	Horizontal shift
Increased blurring from the center	Axial	Skew/Roll

errors in skew also produce a blurring in the vertical direction that results in mixed slices. Finally, random errors in tilt produce blurring proportional to the distance to the center of the FOV (see thick arrows in Figure 7).

3.1.2 | Errors in source-detector distance

Systematic errors in SDD affect the magnification, resulting in an isotropic change of image size (Figure 8).

Positive errors in the SDD have a tighter tolerance (3 mm in all views) than negative errors (5 mm in all views). Random errors led to streaks and blurring with a tolerance of 7 mm in all views.

Systematic errors in SDD proportional to the angular position show blurring with a tolerance of 4 mm in the axial view. The maximum blurring is in the direction perpendicular to the beam when the source is at the angular position where the SDD error is higher (Figure 9). When the error is maximum at 90° and 270° (Scenario 1 in Figure 1), coronal and sagittal views have a tolerance of 4 and 13 mm, respectively, while the tolerance for coronal and sagittal views is 13 and 4 mm, respectively, when the error is maximum at 0° and 180° (scenario 2 in Figure 1).

3.1.3 | Errors in angular position of the gantry

Systematic errors in the angular position of the gantry only result in a rotation of the reconstructed image with no image degradation. Random errors in angular position result in streaks and blurring with a tolerance of 0.25° for all views (Figure 10).

3.1.4 | Errors in the vertical and horizontal position of the detector (vertical and horizontal shift)

The effect of systematic errors in the horizontal position of the detector is the presence of blurring in the three views, with a tolerance of 0.4 mm in the axial view and 0.45 mm in the coronal and sagittal views (Figure 11, top). Random errors produce blurring and streaks in the image with a tolerance of 0.8 mm in the axial view and 0.95 mm in the coronal and sagittal views.

Systematic errors in the vertical position of the detector show a vertical displacement of the sample proportional to the shift, which result in a reduction of the field of view in the longitudinal direction. These errors also produce blurring in all views with a tolerance of 2 mm in the axial view and of 4 mm in the coronal and sagittal views (Figure 11, bottom). Random errors result in streaks and blurring in the axial view with a tolerance of 3.5 and 0.9 mm in the coronal and sagittal views, respectively.

3.1.5 | Errors in the detector roll

Errors in the detector roll show as blurring in all views with a tolerance of 1.5° for the case of systematic errors (Figure 12). Random errors produce blurring and streaks in the image with a tolerance of 2.6° in all views.

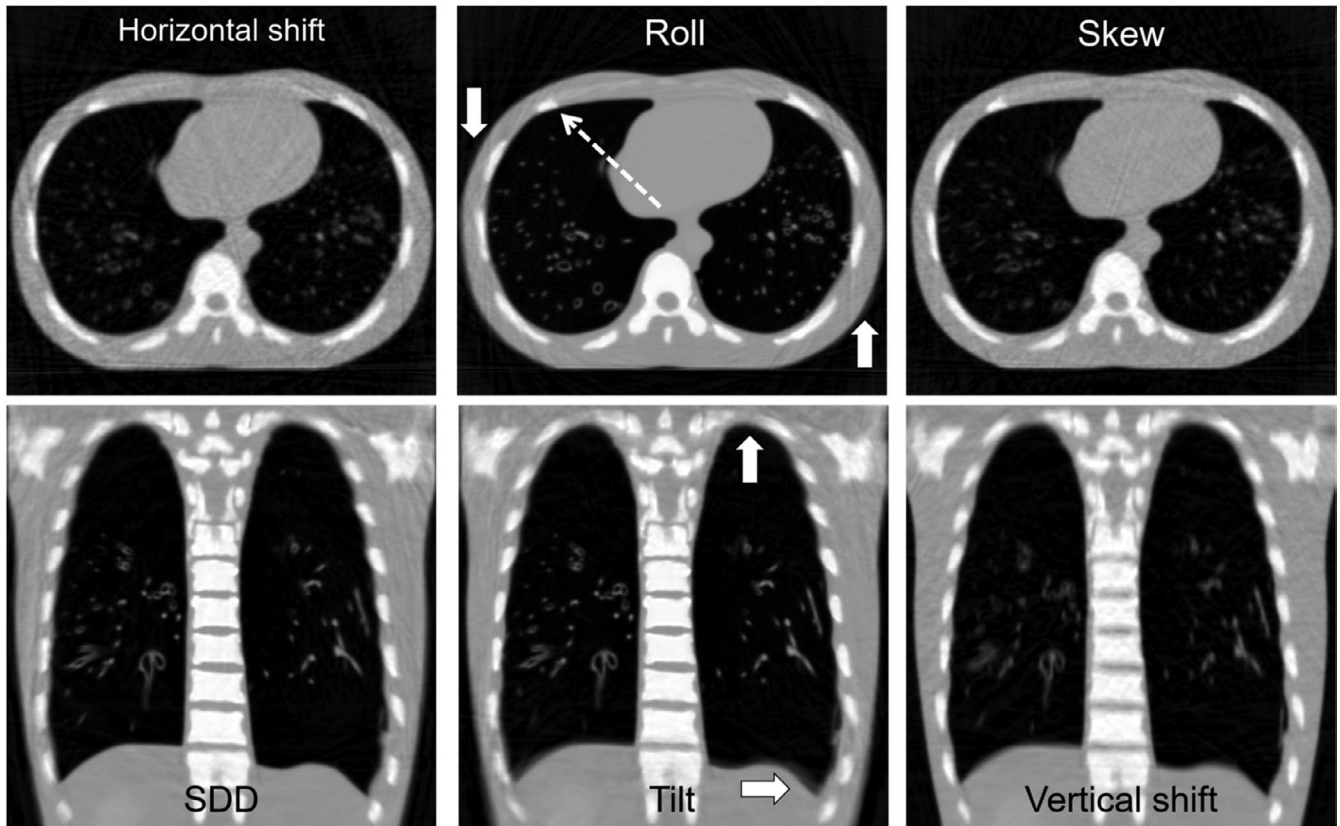


FIGURE 7 Anthropomorphic phantom reconstructed with random errors drawn from a uniform distribution with standard deviation of 2 mm for horizontal shift, 6.5° for roll, 1.5° for skew, 20 mm for SDD, 15° for tilt, and 4 mm for vertical shift. Protocol 1 (voxel size of $394 \mu\text{m}$)

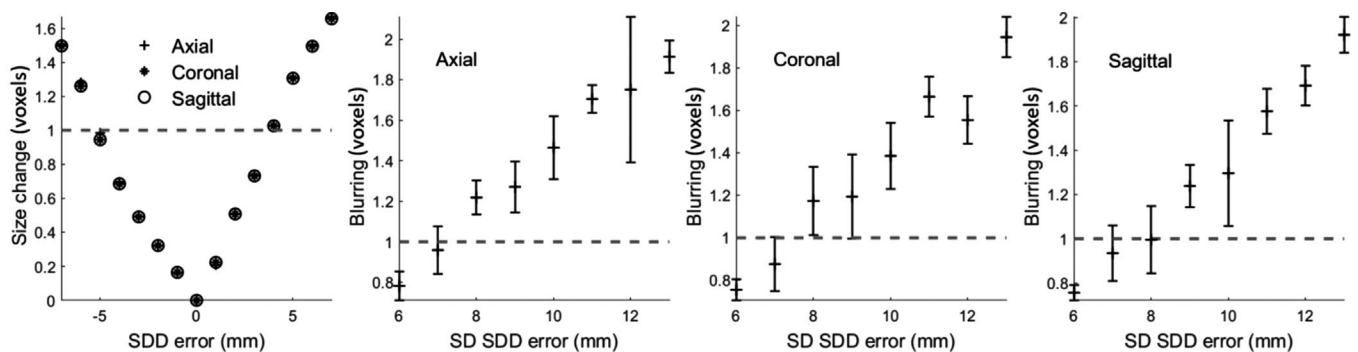


FIGURE 8 Effect on the reconstructed image of systematic and random errors in the source-detector distance (SD stands for standard deviation). Protocol 1 (voxel size of $394 \mu\text{m}$)

3.1.6 | Errors in the detector skew

Errors in the detector skew result in blurring in the axial view, with an effect dependent on the distance to the center of the FOV (Figure 13, top). Tolerance measured at 47.28 mm from the center of the FOV was of 0.3° in the axial view and 0.2° in the sagittal and coronal views for the case of systematic errors. Random errors produce blurring and streaks in the image with a tolerance of 0.6° in the axial view and 0.5° in the coronal and sagittal views.

3.1.7 | Errors in the detector tilt

The effect of systematic errors in the detector tilt was shape distortion in all views, with a dependency on the distance to the FOV center in the longitudinal direction (Figure 13, bottom). Tolerance measured at 47.28 mm from the center of the FOV was of 2° for the axial view and of 4° for coronal and sagittal views (Figure 13, bottom). Random errors showed streaks and blurring with a tolerance of 5.3° in the axial view and 6.4° in the coronal and sagittal views.

The dependency with the distance to the FOV center in the longitudinal direction of errors in skew and tilt results in the different tolerance value for each position shown in Figure 14.

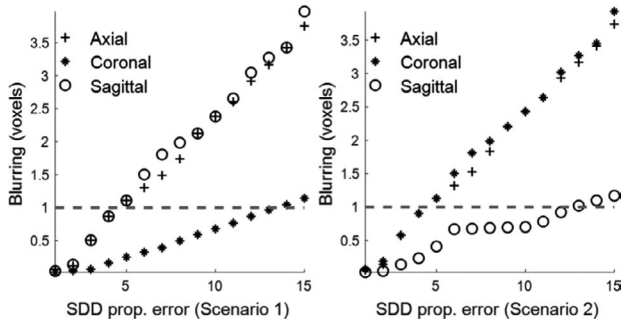


FIGURE 9 Effect on the reconstructed image of errors in SDD proportional to the angular position when the error is maximum at 90 and 270° (left) and when it is maximum at 0 and 180° (right). Protocol 1 (voxel size of 394 μm)

3.1.8 | Summary of estimated tolerances

Table 3 summarizes the tolerances obtained for all geometrical parameters together with the type of undesirable effect produced in the reconstructed image and the views where it is more noticeable.

3.1.9 | Dependency of tolerance with acquisition parameters with influence in the spatial resolution

Left panel of Figure 15 shows the dependency of the tolerance with projection pixel size. Similar linear behavior appeared in the case of random errors. We did not find a relationship between tolerances for the geometrical parameters with angular step, but only streaks due to the lack of angular sampling in protocols 3, 4, and 5. Right panel of Figure 15 shows the tolerances

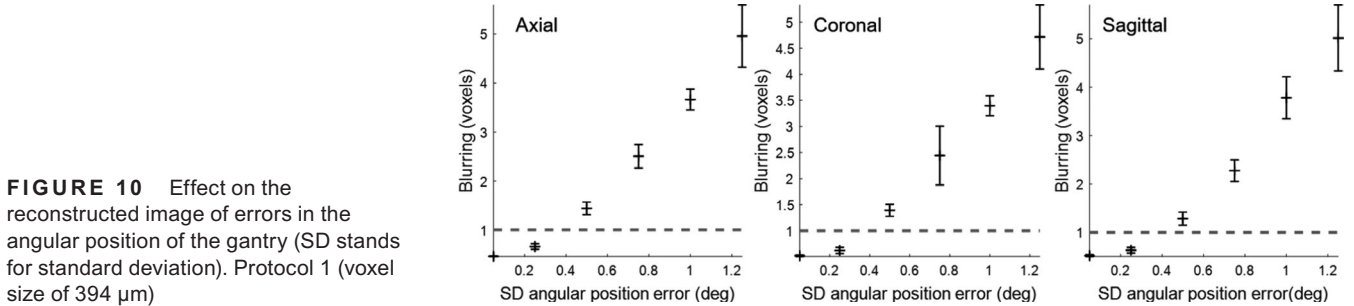


FIGURE 10 Effect on the reconstructed image of errors in the angular position of the gantry (SD stands for standard deviation). Protocol 1 (voxel size of 394 μm)

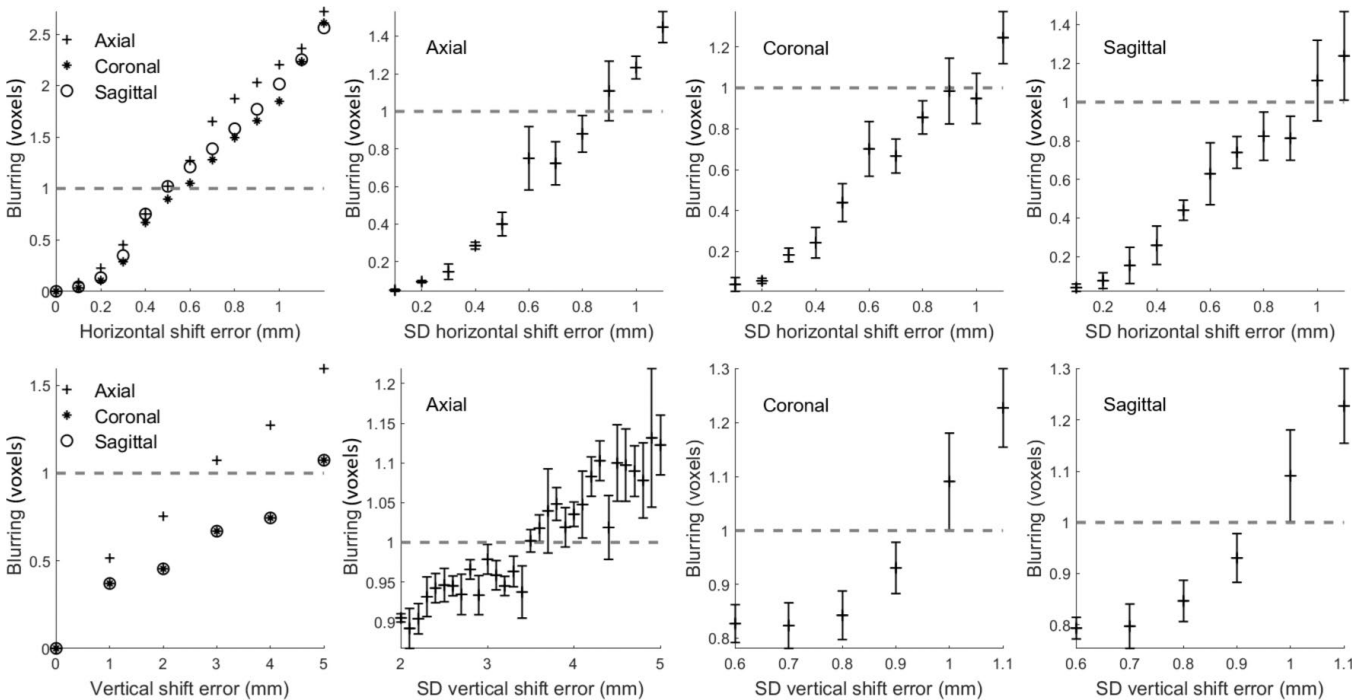


FIGURE 11 Top: Effect on the reconstructed image of systematic and random errors for the horizontal position of the detector. Bottom: Effect on the reconstructed image of systematic and random errors in the vertical position of the detector. SD stands for standard deviation. Protocol 1 (voxel size of 394 μm)

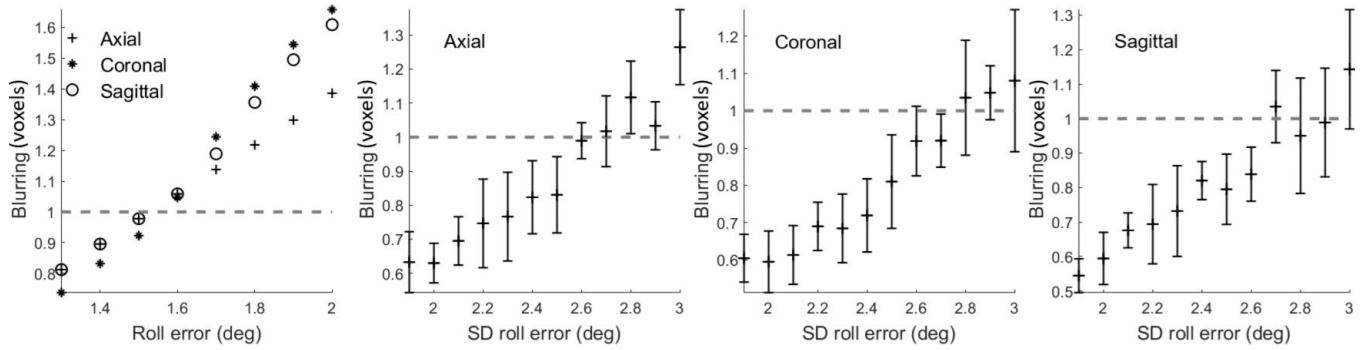


FIGURE 12 Effect on the reconstructed image of systematic and random errors in the detector roll. SD stands for standard deviation. Protocol 1 (voxel size of $394\ \mu\text{m}$)

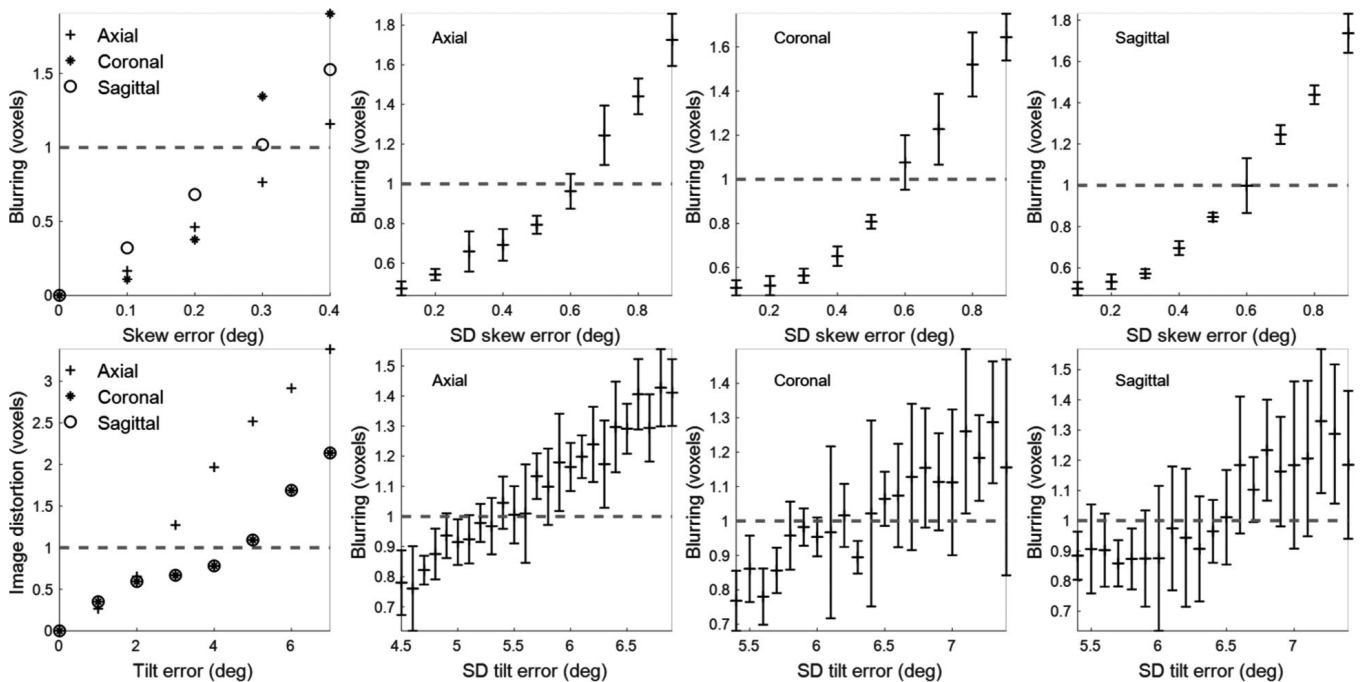


FIGURE 13 Effect on the reconstructed image of systematic and random errors at $47.28\ \text{mm}$ from the center of the FOV for the axial, sagittal and coronal views in the detector skew (top) and tilt (bottom). SD stands for standard deviation. Protocol 1 (voxel size of $394\ \mu\text{m}$)

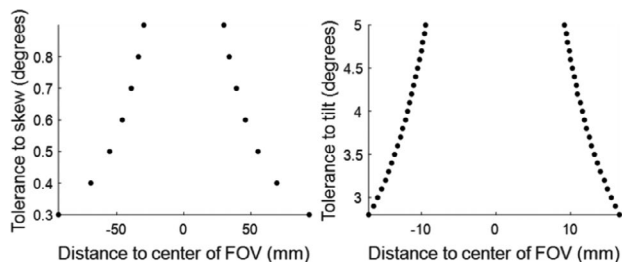


FIGURE 14 Tolerance to systematic errors in the detector skew (left) and tilt (right) as a function of the axial distance to the center of the FOV. Protocol 1 (voxel size of $394\ \mu\text{m}$)

for three system magnification values. The only parameters that depend on the system magnification are those that involve changes in magnification, that is, tilt, roll, and SDD.

4 | DISCUSSION

This paper presents a comprehensive study, based on realistic simulations, of the effects on image quality produced by a wrong geometrical calibration in CBCT systems. For each geometrical parameter, we identify the visual effects produced in the reconstructed image and estimate its tolerance (in terms of mechanical precision) in a systematic and quantitative way.

Errors in geometrical parameters produce four different effects: (1) size change and (2) shape distortion, which, for example, may hinder size quantification of nodules or tumors, (3) blurring, which affects both size and HU quantification, and (4) displacement, which involves a reduction of the axial FOV. Changes in size are produced by changes in magnification, which is

TABLE 3 Summary of tolerances. A, C, S stand for axial, coronal and sagittal views. (a) indicates a dependency with the distance to the rotation axis, (b) indicates a dependency with the distance to the center of the axial plane, and (c) indicates that the value was taken at 47,28 mm from the FOV center

	SYSTEMATIC ERRORS					RANDOM ERRORS				
	Effect	A	C	S	Tolerance	Effect	A	C	S	Tolerance
SDD	Size change	x	x	x	3 mm	Blurring and streaks	x	x	x	7 mm
SDD proportional	Blurring (a)	x		x	4 mm	—				—
	Blurring (a)		x		13 mm					
Angular position	Rotation	x			-	Blurring and streaks	x	x	x	0.25°
	Blurring	x			2 mm	Blurring and streaks	x			3.5 mm
Vertical shift	Blurring		x	x	4 mm	Blurring and streaks		x	x	0.9 mm
	Blurring	x			0.4 mm	Blurring and streaks	x			0.8 mm
Horizontal shift	Blurring		x	x	0.5 mm	Blurring and streaks		x	x	0.95 mm
	Blurring (a)	x	x	x	1.5°	Blurring & streaks (a)	x			2.6°
Roll	Blurring (a)					Blurring & streaks (a)		x	x	2.65°
	Blurring (b)	x			0.3° (c)	Blurring & streaks (b)	x			0.6° (c)
Skew	Blurring (b)		x	x	0.2° (c)	Blurring & streaks (b)		x	x	0.5° (c)
	Shape distortion (b)	x			2° (c)	Blurring & streaks (b)	x			5.3° (c)
Tilt	Shape distortion (b)		x	x	4° (c)	Blurring & streaks (b)		x	x	6.4° (c)

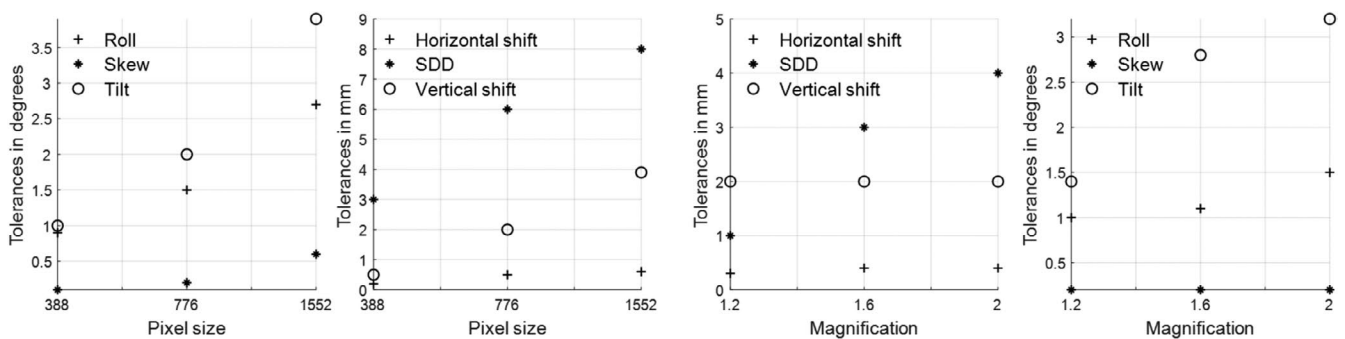


FIGURE 15 Dependence of the tolerance to errors in geometrical parameters with the pixel size (acquisition protocols 2, 6, and 7), with values for skew and tilt measured in the axial slice at 47.28 mm from the center) and with the magnification (acquisition protocols 7 and 8)

modeled in this work as an error in SDD. Errors in tilt produce a distortion that varies from shrinking to enlargement along the longitudinal direction. The blurring effect is associated to horizontal and vertical shifts, skew, and roll. Errors in horizontal shift can be identified as a 2D isotropic blurring in the axial view constant across slices, while errors in vertical shift produce a vertical blurring increasing with the distance to the rotation axis together with a displacement of the

object in the vertical direction. Skew errors produce a 3D blurring: 2D isotropic blurring in the axial view that increases with the distance to the center of the FOV together with a non-isotropic blurring in longitudinal direction with a mixing of slices. Roll errors produce an increasing blurring with respect to the distance of the rotation axis. Proportional errors in SDD due, for example, to the weight of the x-ray tube in C-arms, cause a 3D blurring that increases with the distance to the

rotation axis and is higher in the direction perpendicular to the projection angles with higher SDD errors. Systematic errors in the angular position cause only a rotation of the whole image with no artifacts.

Tolerance for systematic errors that affect the detector position in the tangential direction of the system rotation, that is, skew (0.2°) and horizontal shift (0.4 mm), is tighter than that for those affecting to the longitudinal direction (vertical shift: 2 mm) or the magnification (roll: 1.5° , tilt: 2° and SDD: 3 mm).

This work provides a guideline to identify the most predominant sources of error based on the effects shown in the reconstructed image, which can be summarized in two steps. First, we evaluate coronal or sagittal view: if the effect is mainly visible at the top and bottom of the image, it is due to the tilt error; if it is a blurring mainly at the right and left edges of the image, it is due to a roll error; if it is a 2D blurring, higher with the distance to the center, it is due to a skew error; if it is only a vertical or horizontal blurring, it is due to a vertical or horizontal shift error, respectively. In a second step, the evaluation of axial view enables to confirm the previous assessment: if the effect is a 2D isotropic blurring, it is due to a horizontal shift or skew; if it is a blurring that increases with respect to the center of the image, it is due to roll error.

As the random errors introduce positive and negative values around zero, they only cause inconsistencies in the projection domain that lead to blurring and streaks in all cases. Tolerance to random errors in those parameters for which systematic errors also produce blurring (horizontal shift, skew, vertical shift, and roll) is twice that of the systematic case. Tolerance to random errors in those parameters for which systematic errors produce distortion with no blurring (tilt) is three times that of the systematic case. The identification of the sources of error follows the same steps described for the systematic errors.

Results of this work can be translated to other CT systems based on cone-beam geometry, considering the dependence of the tolerance with: (1) angular step: none found; (2) pixel size: tolerance for all parameters increases linearly with detector pixel size, as it implies a reduction of the spatial resolution, which hinders the visibility of the errors in the reconstructed image; and (3) magnification: tolerance for those errors that modify magnification (roll, tilt, and SDD) is inversely proportional to the system magnification, as the relative error is more significant for smaller system magnifications (no dependency found for horizontal and vertical shifts and skew).

The impact of errors in the geometrical parameters on a specific system will depend on its mechanical tolerance. For example, in a non-motorized C-arm designed for 2D images, as the one used in Abella et al.,²¹ geometrical errors exceed the tolerances in all the cases except for detector roll. In the motorized C-arm systems, with

more accurate mechanics and lower magnification, the only parameter that exceeds the tolerance is the horizontal shift. This may suggest that horizontal shift is the most important parameter in the geometrical calibration, but further confirmation in this regard is warranted.

5 | CONCLUSION

The results of this work could be used to guide the design of new systems, establishing the mechanical precision that must be achieved by the x-ray devices, and to help in the definition of an optimum geometrical calibration process. Also, the thorough visual assessment may be valuable to identify the most predominant sources of error based on the effects shown in the reconstructed image.

ACKNOWLEDGMENT

This work has been supported by Ministerio de Ciencia, Innovación y Universidades, Agencia Estatal de Investigación, project "DPI2016-79075-R - AEI/FEDER, UE", Instituto de Salud Carlos III, project "DTS17/00122", cofunded by European Regional Development Fund (ERDF), "A way of making Europe". Also partially funded by project "DEEPCM-UC3M," funded by the call "Programa de apoyo a la realización de proyectos interdisciplinarios de I+D para jóvenes investigadores de la Universidad Carlos III de Madrid 2019-2020 en el marco del Convenio Plurianual Comunidad de Madrid - Universidad Carlos III de Madrid" and project "RADCOV19," funded by CRUE Universidades, CSIC and Banco Santander (Fondo Supera). The CNIC is supported by the Ministerio de Ciencia, Innovación y Universidades and the Pro CNIC Foundation, and is a Severo Ochoa Center of Excellence (SEV-2015-0505).

CONFLICT OF INTERESTS

The authors declare that they have no conflicts of interest.

DATA AVAILABILITY STATEMENT

All relevant data are available from the Zenodo database, under the DOI: <https://doi.org/10.5281/zenodo.1220275>.

REFERENCES

1. Robb RA. The dynamic spatial reconstructor: an X-ray video-fluoroscopic CT scanner for dynamic volume imaging of moving organs. *IEEE Trans Med Imaging*. 1982;1(1):22-33.
2. Hirota S, Nakao N, Yamamoto S, et al. Cone-beam CT with flat-panel-detector digital angiography system: early experience in abdominal interventional procedures. *Cardiovasc Intervent Radiol*. 2006;29(6):1034-1038.
3. Patel NV, Gounis MJ, Wakhloo AK, et al. Contrast-enhanced angiographic cone-beam CT of cerebrovascular stents: experimental optimization and clinical application. *AJNR Am J Neuroradiol*. 2011;32(1):137-144.

4. Badea CT, Drangova M, Holdsworth DW, Johnson GA. In vivo small-animal imaging using micro-CT and digital subtraction angiography. *Phys Med Biol*. 2008;53(19):R319-R350.
5. Schambach SJ, Bag S, Schilling L, Groden C, Brockmann MA. Application of micro-CT in small animal imaging. *Methods*. 2010;50(1):2-13.
6. Grills IS, Hugo G, Kestfn LL, et al. Image-guided radiotherapy via daily online cone-beam CT substantially reduces margin requirements for stereotactic lung radiotherapy. *Int J Radiat Oncol Biol Phys*. 2008;70(4):1045-1056.
7. Den RB, Doemer A, Kubicek G, et al. Daily image guidance with cone-beam computed tomography for head-and-neck cancer intensity-modulated radiotherapy: a prospective study. *Int J Radiat Oncol Biol Phys*. 2010;76(5):1353-1359.
8. Chen BA, Ning RL. Cone-beam volume CT mammographic imaging: feasibility study. In: Antonuk LE, Yaffe MJ, eds. *Medical Imaging 2001: Physics of Medical Imaging*, vol. 2. Bellingham: Spie-Int Soc Optical Engineering; 2001:655-664.
9. Yao J, Shaw C, Lai CJ, Rong J, Wang J, Liu W. Cone beam CT for determining breast cancer margin: an initial experience and its comparison with mammography and specimen radiograph. *Internat J Clin Experiment Med*. 2015;8(9):15206-15213.
10. Angelopoulos C, Thomas S, Hechler S, Parissis N, Hlavacek M. Comparison between digital panoramic radiography and cone-beam computed tomography for the identification of the mandibular canal as part of presurgical dental implant assessment. *J Oral Maxillofac Surg*. 2008;66(10):2130-2135.
11. Bernardes RA, de Moraes IG, Duarte MAH, Azevedo BC, de Azevedo JR, Bramante CM. Use of cone-beam volumetric tomography in the diagnosis of root fractures. *Oral Surg Oral Med Oral Pathol Oral Radiol Endodontol*. 2009;108(2):270-277.
12. Siewerdsen JH, Moseley DJ, Burch S, et al. Volume CT with a flat-panel detector on a mobile, isocentric C-arm: pre-clinical investigation in guidance of minimally invasive surgery. *Med Phys*. 2005;32(1):241-254.
13. Khoury A, Siewerdsen JH, Whyne CM, et al. Intraoperative cone-beam CT for image-guided tibial plateau fracture reduction. *Computer Aided Surgery*. 2007;12(4):195-207.
14. Schafer S, Nithianathan S, Mirotu DJ, et al. Mobile C-arm cone-beam CT for guidance of spine surgery: image quality, radiation dose, and integration with interventional guidance. *Med Phys*. 2011;38(8):4563-4574.
15. King E, Daly MJ, Chan H, et al. Intraoperative cone-beam CT for head and neck surgery: feasibility of clinical implementation using a prototype mobile C-arm. *Head Neck-J Sci Specialties Head Neck*. 2013;35(7):959-967.
16. Kenngott HG, Wagner M, Gondan M, et al. Real-time image guidance in laparoscopic liver surgery: first clinical experience with a guidance system based on intraoperative CT imaging. *Surg Endoscopy Intervent Techniq*. 2014;28(3):933-940.
17. Daly MJ, Siewerdsen JH, Cho YB, Jaffray DA, Irish JC. Geometric calibration of a mobile C-arm for intraoperative cone-beam CT. *Med Phys*. 2008;35(5):2124-2136.
18. Ferrucci M, Ametova E, Carmignato S, Dewulf W. Evaluating the effects of detector angular misalignments on simulated computed tomography data. *Precis Eng*. 2016;45:230-241.
19. Muralikrishnan B, Shilling M, Phillips S, Ren W, Lee V, Kim F. X-ray computed tomography instrument performance evaluation, part I: sensitivity to detector geometry errors. *NIST J Res*. 2019; submitted.
20. Abella M, Serrano E, Garcia-Blas J, et al. FUX-Sim: An implementation of a fast universal simulation/reconstruction framework for X-ray systems. *PLoS ONE*. 2017;12(7):e0180363.
21. Abella M, de Molina C, Ballesteros N, et al. Enabling tomography with low-cost C-arm systems. *PLoS ONE*. 2018;13(9):e0203817.

How to cite this article: Abella M, Martinez C, Garcia I, Moreno P, De Molina C, Desco M. Tolerance to geometrical inaccuracies in CBCT systems: A comprehensive study. *Med Phys*. 2021; 48:6007–6019. <https://doi.org/10.1002/mp.15065>